**Article:**
Routledge, T.J., Stringer, M., Game, O.S. et al. (2019) Low-temperature, high-speed reactive deposition of metal oxides for perovskite solar cells. Journal of Materials Chemistry A, 7 (5). pp. 2283-2290. ISSN: 2050-7488

https://doi.org/10.1039/c8ta10827g

# Low-Temperature, High-Speed Reactive Deposition of Metal Oxides for Perovskite Solar Cells

Thomas J. Routledge[1,α], Michael Wong-Stringer[1,α], Onkar S. Game[1], Joel A. Smith[1], James E. Bishop[1], Naoum Vaenas[1], Benjamin G. Freestone[1], David M. Coles[1], Trevor McArdle[2], Alastair R. Buckley[1] and David G. Lidzey[1,*]

[1]Department of Physics & Astronomy, University of Sheffield, Hicks Building, Hounsfield Road, Sheffield, S3 7RH, United Kingdom

[2]Power Roll Limited, Washington Business Centre, 2 Turbine Way, Sunderland, SR5 3NZ, United Kingdom

[α]These authors contributed equally to this work

*Corresponding author, email d.g.lidzey@sheffield.ac.uk

Keywords: perovskite solar cells, metal oxide, NiO, nickel oxide $TiO_2$, titanium dioxide electron-beam evaporation, reactive, scalable, low-temperature.

## Abstract

Nickel oxide (NiO) and titanium dioxide ($TiO_2$) charge-extraction layers are fabricated under a partial pressure of $O_2$ from nickel and titanium metals using a reactive electron-beam evaporation process. Using such materials, inverted architecture perovskite solar cells incorporating a NiO hole-transport layer achieve power conversion efficiencies up to 15.8 %, whilst standard architecture devices using a $TiO_2$ electron-transport layer achieve a power conversion efficiency up to 13.9 %. Critically, we find that such metal oxides can be deposited at high speed (nm/s) and at low substrate-temperature, and do not require a high-temperature anneal step after deposition, making reactive electron-beam evaporation compatible with roll-to-roll processing on sensitive flexible polymeric substrates.

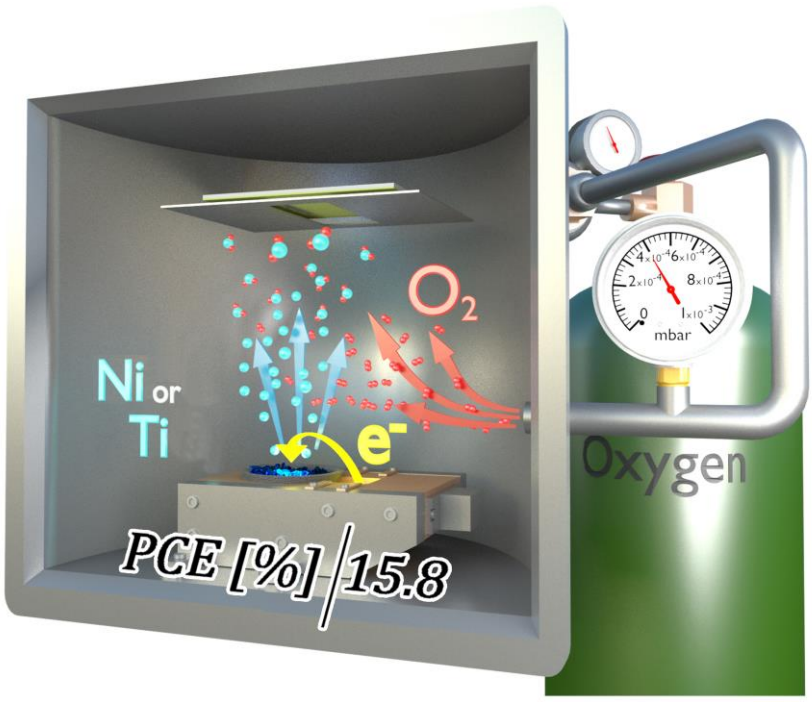


## Introduction

The efficiency of perovskite solar cells (PSCs) has increased rapidly, with recently reported power conversion efficiencies (PCEs) commonly exceeding 20 %.[1,2] Such advances have been driven by the synthesis of new perovskite materials, and by the development of superior charge-transporting materials. Indeed, high PCE PSCs are reliant on the use of charge-transporting materials that have high conductivity (leading to low resistance losses) and good charge selectivity (leading to low parasitic losses). This role is currently dominated by small molecules and thin polymer films that have been chemically-doped to achieve high conductivities.[3–6] It is known that these dopants can undergo migration within a PSC, resulting in reduced device stability.[4,7] For this reason, there is growing interest in the development of metal oxides for use as charge-transporting layers in PSCs. Such materials (which are free from mobile dopants) can be used to create efficient PSCs, and crucially, have increased thermal and photo-chemical stability compared to their doped organic counterparts.[8–15] Unfortunately, many metal oxides are prepared using high-temperature processes to create effective charge-extraction materials.[9,16–24] While this is not problematic when fabricating devices on substrates such as fluorine-doped tin oxide (FTO) coated glass, it is an issue for device fabrication on polymeric substrates (e.g. polyethylene terephthalate) that are often used in high throughput roll-to-roll (R2R) processes.[15]

In this paper, we explore the deposition of the metal oxides NiO and $TiO_2$ using a reactive electron-beam (e-beam) evaporation technique that is compatible with the low temperature requirements of flexible polymeric substrates. $TiO_2$ and NiO are of significant interest for applications in PSCs due to their favourable conduction and valance band (CB and VB) energies, reported from -3.6 to -4.2 eV and -5.0 and -5.5 eV respectively.[10,13,25–32] These values align with the conduction and valance bands of many ubiquitous perovskites active layers.[10,13,25–32] The high CB of NiO (1.85 eV)[33] and deep VB of $TiO_2$ (7.2 eV)[32] also make them effective at blocking electrons and holes respectively. For this reason, $TiO_2$ and NiO have been used as effective electron- and hole-transporting materials (ETM/HTM) in high-performance PSCs. Here, we deposit $TiO_2$ and NiO using a process that utilises metallic pellets which are evaporated using an electron-beam, with an oxygen partial pressure within the deposition chamber oxidising the vaporized metals. We show that this process is compatible with high-speed R2R manufacturing by fabricating efficient PSCs in which the metal oxide charge-transporting layers were deposited at rates up to 1 nm/s.

We note that a number of alternative processes have been used to deposit NiO and $TiO_2$, however many of these techniques have issues with manufacture scalability. For example NiO and $TiO_2$ have previously been deposited from sol-gel or nanoparticle suspensions,[20,22,26,27,33–36] using chemical bath deposition (CBD), atomic layer deposition (ALD), magnetron sputtering, pulsed laser deposition and e-beam deposition. However techniques such as CBD require elevated temperatures either during[37] or post deposition.[8] Such temperatures can be reduced below 100 °C, although this is at the cost of extended reaction times, thereby reducing the capacity for R2R deposition.[38] Slow deposition rates are also a major limitation of ALD; indeed $TiO_2$ films deposited via ALD can take up to 100 minutes (over 200 cycles) to form a 20 nm layer.[11] Despite their potential for scalability, metal oxide films deposited from nanoparticle solutions usually contain residual organic ligands or stabilisers that cannot be removed by low temperature annealing.[39] This issue can be avoided by depositing a metallic film (e.g. Ni) which is then oxidized using a post-deposition high-temperature anneal in air to create a HTM.[23,24] Alternatively NiO or $TiO_2$ can be directly deposited from stoichiometric source pellets using techniques such as magnetron sputtering, pulsed laser or e-beam deposition.[12,25,30,33,40–45] However the interaction of source metal oxide pellets with high-

energy electron beams, lasers or plasmas quickly changes their initial stoichiometry, leading to batch-to-batch inconsistencies in the optical and electronic properties of the resultant oxide-materials.

In contrast, the reactive e-beam technique used here to produce metal oxides is inherently low-cost in nature,[10,46,47] and combines both reduced substrate temperature, and high-speed deposition. It is therefore well suited for R2R fabrication. Using this technique, we demonstrate the fabrication of inverted architecture (p-i-n) PSCs with NiO, and standard architecture (n-i-p) PSCs with $TiO_2$, and report champion PCEs of 15.8 % and 13.9 % for PSCs incorporating NiO and $TiO_2$ respectively. We also fabricate PSCs with a PCE of 14.2 % (NiO) and 13.5 % ($TiO_2$) when using a fast (1 nm/s) deposition rate. Finally, we demonstrate that this technique can also be used to create devices that require no thermal annealing (i.e. all process steps are carried out at room temperature), with $TiO_2$-based PSCs achieving a PCE of 11.3 %. We emphasize that the use of a vacuum in this process is not expected to present a barrier to manufacture, as vacuum-deposition techniques are well established in R2R processing; e.g. the production of low-cost metallized plastic for food packaging applications.[48]

**Results and discussion**

The reactive e-beam process used to deposit NiO and $TiO_2$ is detailed in Figure 1a. Metal pellets were placed in a deposition crucible and melted using an electron-beam, while oxygen gas was bled into the chamber at a partial pressure from $5x10^{-5}$ mbar to $1.9\ x10^{-4}$ mbar. The oxygen gas oxidised the evaporating metal-vapour, resulting in the deposition of a metal oxide film onto the substrate (here a patterned indium tin oxide [ITO] electrode). Evaporation rates were adjusted through control of beam current, with film deposition rates (measured using a quartz-crystal microbalance) between 0.3 and 10 Å/s utilised. To understand the deposition-process in more detail, we have used temperature-sensitive label indicators to directly monitor the temperature of the substrates. This measurement indicated that the temperature of the substrate did not exceed 70 °C at any point during deposition, confirming that this process is in principle compatible with sensitive polymeric-substrates.

We have also investigated the effect of exposing such metal oxide films to a 15-minute UV-ozone treatment immediately before perovskite deposition. Inverted architecture (p-

i-n) PSCs were fabricated based on the structure ITO/NiO/perovskite/$PC_{60}BM$/bathophenanthroline (BPhen)/Ag as shown in Figure 1b. Standard-architecture (n-i-p) PSCs were fabricated using the structure ITO/$TiO_2$/perovskite/spiro-OMeTAD/Au as shown in Figure 1c. Further fabrication and measurement details are provided in the supplementary information.

Metal oxide films on ITO were used to create PSC devices using two different perovskite materials. The first was a triple cation perovskite $CsI_{0.05}((FAPbI_3)_{0.83}(MAPbBr_3)_{0.17})_{0.95}$ (referred to as TC), which has been widely used in the literature since it was first used to create devices having a PCE of 21 %.[49] The second perovskite used was the material $MAPbI_3$, which was deposited from an acetonitrile solution (referred to as AC). This process route was first reported by Noel *et al*.[50] and can be used to create highly compact and uniform perovskite films. The devices fabricated were characterised using current-voltage (J-V) sweeps under calibrated 100 mW/cm$^2$ AM1.5 irradiation. Additional characterisation techniques are also employed to explore the optoelectronic and morphological properties of the metal oxide films, including atomic force microscopy (AFM), UV-vis absorption, x-ray diffraction (XRD), X-ray photoelectron spectroscopy (XPS), and spectroscopic ellipsometry.

We first discuss the optical and morphological properties of the films that were deposited. Here, films were deposited on quartz-coated glass at an oxygen partial pressure of 1 x $10^{-4}$ mbar at a rate of 1.5 - 2 Å/s and had an average thickness of 10 nm. Figure 2a, 2b and 2c presents AFM topographs of ITO, NiO and $TiO_2$ respectively. These indicate an RMS roughness of 2.17 nm, 1.69 nm, and 2.03 nm for ITO, NiO and $TiO_2$ respectively. It is apparent that such films do not planarise the ITO substrate, however as they reduce RMS roughness, it is likely that they form a semi-conformal coating.

To further understand the physical structure of the films, XRD measurements were performed on 100 nm thick metal oxide films deposited on quartz-covered glass, with typical data shown in Figure 2d. Here a reference scan recorded on a quartz-coated glass substrate is included for reference. XRD measurements of the NiO film identify crystalline components as evidenced by the appearance of reflections observed at 37° and 63° respectively. Here, the peaks at 37° and 63° coincide with the (111) and (220) reflections, however the expected (200) peak at 43° coincides with a large background peak from the quartz substrate that is apparent at the same angle. To determine whether the (200)

peak contributes to the measured NiO XRD spectra, we have determined the full width at half maximum (FWHM) linewidth of the peaks around 43° in both the quartz-reference and in the NiO-coated quartz-glass. In both cases, we find the linewidth of these peaks to be very similar (quartz $FWHM_{43°}$ = 0.34° ± 0.04° and NiO $FWHM_{43°}$ = 0.31° ± 0.04°), suggesting that that any scattering from the (200) plane-direction is very weak. We note that previous work by Park *et al* [25] used the relative ratio of the (111) and (200) scattering features in NiO films to evidence preferential alignment of crystal planes. Here, we believe that the apparent absence of the expected NiO (200) diffraction peak also suggests a preferential alignment of NiO crystallites along the (111) plane direction. In contrast, we find no clear crystal reflections are observed from $TiO_2$ (the positions where the (101) and (200) reflections are expected are also shown). This indicates that such $TiO_2$ films are largely amorphous.

Figure 2e shows the optical transmission of 10 nm thick NiO and $TiO_2$ films. We find that such films have high optical transmissivity (> 90 %) across the visible spectrum; a favourable property that is likely to reduce parasitic optical absorption in a PV device that would otherwise causes losses in photocurrent. To determine the optical band-gap of the materials deposited, the optical transmission measurements were taken of films that were significantly thicker (100 nm) than would be used in a practical device. This was then used to produce Tauc plots (see Figure S1) from which we determine optical band gaps of (3.64 ± 0.04) eV and (3.61 ± 0.04) eV for NiO and $TiO_2$ respectively. In Figure S2a and S2b we present the refractive index, *n*, obtained for 10 nm NiO and $TiO_2$ films as determined by ellipsometry. Here a Cauchy model was used to confirm film thickness of 10 nm.

We have also characterised the elemental composition of NiO and $TiO_2$ films using XPS, with data presented in Figure S3 and Figure S4. Here, full survey scans (parts a and b) as well as high-resolution metal 2p (parts c and d) and O 1s (parts e and f) spectra of both NiO and $TiO_2$ are provided. These spectra closely match those of previous XPS studies performed on NiO and $TiO_2$,[18,51–54] and indicate that there is no oxygen deficiency in either e-beam deposited materials. Taken together, our characterisation of the reactive e-beam deposited metal oxide films demonstrate that the NiO films are semi-crystalline and the $TiO_2$ films are largely amorphous, with the optical properties of both closely matching that of previous reports of low temperature processed metal oxides.[40–42]

We now consider the application of the metal oxide films created as HTM and ETM materials. Firstly, we discuss the effect of film thickness on device performance. Inverted architecture p-i-n PSC devices were fabricated utilising an AC perovskite with two different thicknesses (10 and 20 nm) of NiO. Table 1 tabulates key device metrics including PCE, fill factor (FF), short circuit current density ($J_{SC}$), open circuit voltage ($V_{OC}$), shunt resistance ($R_{SH}$), and series resistance ($R_S$) for the two thicknesses. Characteristic J-V curves from PSCs are presented in Figure S5a. We find that PSCs containing a 10 nm thick NiO (deposited at 1 Å/s) had a 60 % lower $R_S$ than equivalent devices containing a 20 nm thick film, and similar $R_{SH}$ values. This resulted in an overall PCE enhancement of around 10 % for PSCs containing a 10 nm NiO layer compared to those containing thicker NiO. It is therefore apparent that the thicker NiO films introduced series losses via its limited conductivity. For this reason, 10 nm thick metal oxide films were used in all devices described below.

PSCs with p-i-n configuration were fabricated using a TC perovskite and a NiO HTM. Interestingly, it was found that when the TC perovskite is converted using an anneal temperature of 100 °C (a standard process condition for this material), devices had a relatively poor performance, with low FF (<50 %) and $J_{SC}$ (<16 mA/cm$^2$) leading to a PCE of <6 % (see characteristic J-V curves in Figure S5b). However, such metrics improve significantly when the TC perovskite was instead annealed at a lower temperature (80 °C) in vacuum – see Figure 3a. Using an 80 °C vacuum anneal for inverted architecture PCSs and a standard 100 °C anneal for standard architecture PSCs, we then explored (i) a range of $O_2$ partial pressures ($5x10^{-5}$ mbar, $1x10^{-4}$ and $1.9 x10^{-4}$ mbar) during the metal oxide depositions, and (ii) different evaporation rates (0.5 Å/s and 1.5 or 2 Å/s), with all data presented in Table S1. It was found that across all oxygen partial pressures TC PSCs had similar performance metrics and efficiencies; a result that suggests the deposition process could be easily transferred between different e-beam systems.

We have also explored the effect of exposing the metal oxide films to a UV-Ozone (UVO) treatment for 15 minutes before the perovskite was deposited. This low-temperature and scalable technique is well known to modify surface energy and improve the wettability of materials deposited upon its surface. UVO treatment has also previously been reported to change the stoichiometry of metal oxides by introducing Ni vacancies in NiO[54], oxygen vacancies in $TiO_2$[55] and to induce the formation of NiO(OH) (nickel oxide hydroxide) and

$Ni(OH)_2$ (nickel hydroxide) in NiO films.[51,54,56] Figure 3b presents data for PSCs that contain a TC perovskite, with devices utilising either a NiO HTM or a $TiO_2$ ETM. Characteristic J-V curves of devices used to collect the data are shown in Figure S6a. A vacuum anneal is used to convert the perovskite for all NiO based inverted PSCs for the reasons discussed above.

We firstly discuss the effect of UVO on the NiO HTM; it is found that all device performance metrics are significantly reduced when NiO films are exposed to the UVO (PCE falls from 12 % to 5 % as a result of reduction in both FF and $J_{sc}$). A reduction in the optical transmission of the NiO across all wavelengths (see Figure S6b), with a greater reduction in transmission occurring for a thicker film, coupled with a reduction in its apparent optical band gap by 120 meV (see Figure S1) suggests a change in the stoichiometry of the film.

High resolution XPS scans of Ni 2p spectra reveal an increase in $Ni^{3+}$ relative to $Ni^{2+}$ after UVO treatment (see Figure S3c and S3d), a result consistent with an increase in Ni vacancies or the incorporation of $Ni_2O_3$ or NiO(OH) into the film. A peak in the O 1s spectra that is associated with $OH^-$ is also observed to increase after UVO treatment (see Figure S3e and S3f). As $Ni_2O_3$ and NiO(OH) are optically 'black', their formation is consistent with the loss in transmission observed in NiO film after UVO treatment. The NiO films are only 10 nm thick, therefore it is likely that such states are located through the entire film, resulting in a reduction in device performance as observed for UVO treated NiO HTMs.

We now consider the effect of UVO treatment on the $TiO_2$ ETM. Here, we find that a 15-minute UVO exposure improves the average device PCE from 7.5 % to 10.5 %, with all metrics (particularly FF) increasing. It appears that the UVO process results in an increase in the optical transmittance of $TiO_2$ (see Figure S6c). It is also likely that this process improves the wettability of the perovskite to the $TiO_2$ surface via a reduction in the surface energy, improving the quality of the resultant interface. Our XPS measurements indicate that the UVO treatment results in a significant reduction in contaminants but does not significantly change the stoichiometry of the $TiO_2$. Here O 1s spectra (see Figure S4e and S4f), indicate that a shoulder associated with $OH^-$ contamination is apparently suppressed after UVO treatment. The full survey scan spectrum also directly indicates that UVO removes sodium, potassium and phosphate

contaminants. Note, however that we find no changes in the XRD diffraction spectra of $TiO_2$ and NiO following UVO treatment, suggesting that this process does not result in any substantive change in film crystallinity (See Figure S7).

In Figure 4 we present current-voltage curves of our champion PSCs. Here n-i-p architecture PSCs are prepared with the $TiO_2$ exposed to a UVO for 15 minutes before the deposition of either AC or TC perovskites, with the perovskite films then annealed at 100 °C for 60 minutes. Both AC and TC perovskites were also processed in p-i-n architecture with an NiO HTM. Here UVO treatment was not applied to the NiO, and after TC perovskite deposition the devices were annealed under vacuum at 80 °C (with AC perovskite annealed at 100 °C). We also make use of a multi-layer encapsulation technique, which we have previously demonstrated to increase and stabilise the photocurrent of AC based inverted PSCs.[57] We present the performance metrics of all PSCs discussed in Table 2. Here, standard n-i-p PSCs (Figures 4a and 4b) and inverted p-i-n PSCs (Figure 4c) achieve a maximum PCE of 13.9 % and 15.8 % respectively. We find that the champion PSC using NiO has an impressive FF of 80 %, although the $J_{SC}$ is below 19 mA/cm$^2$.

Previous reports on inverted PSCs utilising NiO as a HTM have shown that the choice of solvent and perovskite stoichiometry (particularly the DMSO:$PbI_2$ ratio), is critical in creating large, columnar perovskite crystal grains.[58] We expect that further optimisation of the perovskite deposition process on NiO fabricated by reactive e-beam is likely to lead to further increases in photocurrent in our inverted PSCs. Furthermore, we note that our champion PSCs did not achieve $V_{OC}$ values exceeding 1.06 V; a result that may be consistent with a preferential orientation as suggested by XRD measurements. We expect that selective doping of the nickel source with either cobalt, magnesium or copper may offer a route to increase the $V_{OC}$ of inverted PSCs by lowering the NiO valence band energy.[14,20,28,59]

Our measurements suggest that devices containing a $TiO_2$ ETM are characterised by high series resistance that limits the FF and PCE. Here such effects may either result from a lack of oxygen vacancies (required for n-type doping) as indicated by the XPS measurements, or may originate from the largely amorphous nature of the $TiO_2$. It is apparent that the UVO exposure used considerably improves the performance of such devices, and we believe that additional (low-temperature) surface treatments of reactive e-beam deposited $TiO_2$ may allow us to achieve some additional crystallization of the $TiO_2$

and further improve its conductivity. Further tuning of the density of oxygen vacancies by optimising the reactive evaporation deposition conditions may also result in a reduction in the electronic barrier to electron extraction.

We have also used our process to explore the rate at which metal oxide films can be deposited and still retain their electronic functionality. Here, NiO and $TiO_2$ layers were fabricated at a high deposition rate of 1 nm/s, with such films then used as charge-extraction layers in PSC devices incorporating a TC perovskite. The current-voltage curves of champion PSCs with these rapidly deposited metal oxides are shown in Figures 4b and 4c, with accompanying device metrics presented in Table 2 (averages and standard deviation are listed in Table S1). We find that PSCs incorporating rapidly deposited metal oxides have PCEs that are equivalent to those obtained with slowly deposited metal oxides. This suggests that the deposition of metal oxides via reactive e-beam is compatible with a high-speed R2R manufacture process.

Finally, we have explored whether it is possible to fabricate PSC devices by removing all annealing steps in the device fabrication route entirely. Figure 4a presents a J-V curve of a standard architecture PSC incorporating a 10 nm thick largely amorphous $TiO_2$ ETM, and an AC $MAPbI_3$ perovskite that was not thermally annealed. Using this route, we achieve a reasonable device PCE of 11.3 %.

**Conclusions**

We have used a reactive electron-beam evaporation process to deposit two different metal oxides from a metal source material under a low partial pressure of oxygen. We find that NiO and $TiO_2$ deposited using this technique can be used to efficiently extract charge from perovskite solar cells, realising peak efficiencies of 15.8 % for inverted structure PSCs using a NiO HTM, and 13.9 % for standard structure PSCs using a $TiO_2$ ETM. We show that control of deposition parameters, choice of perovskite annealing routine and the use of UV-ozone treatment applied to the metal oxides affects the performance metrics of the PSCs created. Critically, our low-temperature deposition process is compatible with sensitive, flexible polymeric substrates, as we demonstrate that reactive electron-beam deposited metal oxides do not need high temperature annealing to function as effective charge-transporting materials. Our work suggests therefore that metal oxide films can be deposited quickly, ensuring that the process is

compatible with high throughput roll-to-roll manufacturing. Indeed, we have recently found that this technique can be successfully implemented onto flexible PET substrates. It is an open question as to whether metal oxide films prepared using this rapid processing method have similar adhesion properties compared to comparable materials prepared using more conventional deposition techniques. Indeed, our future work will address this issue, and will determine the extent to which such materials can be used in more demanding applications in which device stability is limited by thin-film mechanical properties and delamination effects.

**Acknowledgments:** This work was funded by the UK Engineering and Physical Sciences Research Council (EPSRC) via grants EP/M025020/1 'High resolution mapping of performance and degradation mechanisms in printable photovoltaic devices' and EP/M014797/1 'Improved Understanding, Development and Optimization of Perovskite-based Solar Cells', and EP/I032541/1 'Solar Energy in Future Societies'. We also thank the U.K. EPSRC for PhD studentships via the University of Sheffield DTG account (T.R., J.B) and from the Centre for Doctoral Training in New and Sustainable PV, EP/L01551X/1 (M.S., J.S., B.F.). XPS analysis was performed in the Sheffield Surface Analysis Centre.

**Conflict of Interest:** D.G.L. and A.R.B. are co-directors of the company Ossila Ltd that retail materials used in perovskite photovoltaic research. T.M. is an employee of PowerRoll Ltd who are developing solar cell technology based on perovskites and metal oxides.

## References


1 M. Stolterfoht, C. M. Wolff, Y. Amir, A. Paulke, L. Perdigón-Toro, P. Caprioglio and D. Neher, *Energy Environ. Sci.*, 2017, **10**, 1530–1539.

2 M. Abdi-Jalebi, Z. Andaji-Garmaroudi, S. Cacovich, C. Stavrakas, B. Philippe, J. M. Richter, M. Alsari, E. P. Booker, E. M. Hutter, A. J. Pearson, S. Lilliu, T. J. Savenije, H. Rensmo, G. Divitini, C. Ducati, R. H. Friend and S. D. Stranks, *Nature*, 2018, **555**, 497–501.

3 Z. H. Bakr, Q. Wali, A. Fakharuddin, L. Schmidt-Mende, T. M. Brown and R. Jose, *Nano Energy*, 2017, **34**, 271–305.

4 L. Calió, S. Kazim, M. Grätzel and S. Ahmad, *Angew. Chemie Int. Ed.*, 2016, 2–26.

5 S. Ameen, M. A. Rub, S. A. Kosa, K. A. Alamry, M. S. Akhtar, H. S. Shin, H. K. Seo, A. M. Asiri and M. K. Nazeeruddin, *ChemSusChem*, 2016, **9**, 10–27.

6 M. Wong-Stringer, J. E. Bishop, J. A. Smith, D. K. Mohamad, A. J. Parnell, V. Kumar, C. Rodenburg and D. G. Lidzey, *J. Mater. Chem. A*, 2017, **5**, 15714–15723.

7 D. Wang, M. Wright, N. K. Elumalai and A. Uddin, *Sol. Energy Mater. Sol. Cells*, 2016, **147**, 255–275.

8 J. Sun, J. Lu, B. Li, L. Jiang, A. S. R. Chesman, A. D. Scully, T. R. Gengenbach, Y. B. Cheng and J. J. Jasieniak, *Nano Energy*, 2018, **49**, 163–171.

9 W. Chen, Y. Wu, Y. Yue, J. Liu, W. Zhang, X. Yang, H. Chen, E. Bi, I. Ashraful, M. Grätzel and L. Han, *Science*, 2015, **350**, 944–948.

10 S. Sajid, A. M. Elseman, H. Huang, J. Ji, S. Dou, H. Jiang, X. Liu, D. Wei, P. Cui and M. Li, *Nano Energy*, 2018, **51**, 408–424.

11 Y. Lv, P. Xu, G. Ren, F. Chen, H. Nan, R. Liu, D. Wang, X. Tan, X. Liu, H. Zhang and Z.-K. Chen, *ACS Appl. Mater. Interfaces*, 2018, **10**, 23928–23937.

12 H. Lee, Y. T. Huang, M. W. Horn and S. P. Feng, *Sci. Rep.*, 2018, **8**, 1–10.

13 J. You, L. Meng, T. Bin Song, T. F. Guo, W. H. Chang, Z. Hong, H. Chen, H. Zhou, Q. Chen, Y. Liu, N. De Marco and Y. Yang, *Nat. Nanotechnol.*, 2016, **11**, 75–81.

14 K. Yao, F. Li, Q. He, X. Wang, Y. Jiang, H. Huang and A. K. Y. Jen, *Nano Energy*, 2017,

**40**, 155–162.

15 M. Najafi, F. Di Giacomo, D. Zhang, S. Shanmugam, A. Senes, W. Verhees, A. Hadipour, Y. Galagan, T. Aernouts, S. Veenstra and R. Andriessen, *Small*, 2018, **14**, 1–10.

16 I. Senain, N. Nayan and H. Saim, *Int. J. Integr. Eng.*, 2010, **2**, 29–36.

17 D. Bi, W. Tress, M. I. Dar, P. Gao, J. Luo, C. Renevier, K. Schenk, A. Abate, F. Giordano, J.-P. Correa Baena, J.-D. Decoppet, S. M. Zakeeruddin, M. K. Nazeeruddin, M. Grätzel and A. Hagfeldt, *Sci. Adv.*, 2016, **2**, e1501170–e1501170.

18 B. Mustafa, J. Griffin, A. S. Alsulami, D. G. Lidzey and A. R. Buckley, *Appl. Phys. Lett.*, 2014, **104**, 5.

19 S. Yue, K. Liu, R. Xu, M. Li, M. Azam, K. Ren, J. Liu, Y. Sun, Z. Wang, D. Cao, X. Yan, S. Qu, Y. Lei and Z. Wang, *Energy Environ. Sci.*, 2017, **10**, 2570–2578.

20 J. W. Jung, C. C. Chueh and A. K. Y. Jen, *Adv. Mater.*, 2015, **27**, 7874–7880.

21 I. Sta, M. Jlassi, M. Hajji and H. Ezzaouia, *Thin Solid Films*, 2014, **555**, 131–137.

22 J. Jeng, K. Chen, T. Chiang, P. Lin, T. Tsai, Y. Chang, T. Guo, P. Chen, T. Wen and Y. Hsu, *Adv. Mater.*, 2014, **26,** 4107–4113.

23 W. Lai, K. Lin, T. Guo and J. Lee, *IEEE Trans. Electron Devices*, 2015, **62**, 1590–1595.

24 W. Lai, K. Lin, Y. Wang, T. Chiang, P. Chen and T. Guo, *Adv. Mater.*, 2016, **28,** 3290–3297.

25 J. H. Park, J. Seo, S. Park, S. S. Shin, Y. C. Kim, N. J. Jeon, H. W. Shin, T. K. Ahn, J. H. Noh, S. C. Yoon, C. S. Hwang and S. Il Seok, *Adv. Mater.*, 2015, **27**, 4013–4019.

26 H. L. Zhu, J. Cheng, D. Zhang, C. Liang, C. J. Reckmeier, H. Huang, A. L. Rogach and W. C. H. Choy, *ACS Nano*, 2016, **10**, 6808–6815.

27 U. Kwon, B. G. Kim, D. C. Nguyen, J. H. Park, N. Y. Ha, S. J. Kim, S. H. Ko, S. Lee, D. Lee and H. J. Park, *Sci. Rep.*, 2016, **6**, 1–10.

28 G. Li, Y. Jiang, S. Deng, A. Tam, P. Xu, M. Wong and H. S. Kwok, *Adv. Sci.*, 2017, **4**, 1–8.

29 K. Wojciechowski, M. Saliba, T. Leijtens, A. Abate and H. J. Snaith, *Energy Environ. Sci.*, 2014, **7**, 1142–1147.

30 D. Yang, R. Yang, J. Zhang, Z. Yang, S. Liu and C. Li, *Energy Environ. Sci.*, 2015, **8**, 3208–3214.

31 J. H. Noh, N. J. Jeon, Y. C. Choi, M. K. Nazeeruddin, M. Grätzel and S. Il Seok, *J. Mater. Chem. A*, 2013, **1**, 11842.

32 K. Mahmood, S. Sarwar and M. T. Mehran, *RSC Adv.*, 2017, **7**, 17044–17062.

33 S. Weber, T. Rath, J. Mangalam, B. Kunert, A. M. Coclite, M. Bauch, T. Dimopoulos and G. Trimmel, *J. Mater. Sci. Mater. Electron.*, 2018, **29**, 1847–1855.

34 H. Zhang, J. Cheng, D. Li, F. Lin, J. Mao, C. Liang, A. K. Y. Jen, M. Grï¿½tzel and W. C. H. Choy, *Adv. Mater.*, 2017, **29**, 1–7.

35 H. Zhou, Q. Chen, G. Li, S. Luo, T. Song, H.-S. Duan, Z. Hong, J. You, Y. Liu and Y. Yang, *Sci. (Washington, DC, U. S.)*, 2014, **345**, 542–546.

36 Q. He, K. Yao, X. Wang, X. Xia, S. Leng and F. Li, *ACS Appl. Mater. Interfaces*, 2017, **9**, 41887–41897.

37 K. Yamamoto, Y. Zhou, T. Kuwabara, K. Takahashi, M. Endo, A. Wakamiya, Y. Ogomi, S. Hayase and T. Taima, in *2014 IEEE 40th Photovoltaic Specialist Conference (PVSC)*, IEEE, 2014, pp. 1573–1576.

38 C. Liang, Z. Wu, P. Li, J. Fan, Y. Zhang and G. Shao, *Appl. Surf. Sci.*, 2017, **391**, 337–344.

39 W. Qiu, U. W. Paetzold, R. Gehlhaar, V. Smirnov, H. G. Boyen, J. G. Tait, B. Conings, W. Zhang, C. B. Nielsen, I. McCulloch, L. Froyen, P. Heremans and D. Cheyns, *J. Mater. Chem. A*, 2015, **3**, 22824–22829.

40 S. R. Pae, S. Byun, J. Kim, M. Kim, I. Gereige and B. Shin, *ACS Appl. Mater. Interfaces*, 2017, **10**, 534-540.

41 M. F. Hossain, S. Naka and H. Okada, *J. Photochem. Photobiol. A Chem.*, 2018, **360**, 109–116.

42 W. Qiu, U. W. Paetzold, R. Gehlhaar, V. Smirnov, H.-G. Boyen, J. G. Tait, B. Conings,

W. Zhang, C. Nielsen, I. Mcculloch, L. Froyen, P. Heremans and D. Cheyns, *J. Mater. Chem. A*, 2015, **3**, 22824–22829.

43 C.-H. Wei and C.-M. Chang, *Mater. Trans.*, 2011, **52**, 554–559.

44 J. Cui, F. Meng, H. Zhang, K. Cao, H. Yuan, Y. Cheng, F. Huang and M. Wang, *ACS Appl. Mater. Interfaces*, 2014, **6**, 22862–22870.

45 K. C. Wang, P. S. Shen, M. H. Li, S. Chen, M. W. Lin, P. Chen and T. F. Guo, *ACS Appl. Mater. Interfaces*, 2014, **6**, 11851–11858.

46 Z. Song, C. L. McElvany, A. B. Phillips, I. Celik, P. W. Krantz, S. C. Watthage, G. K. Liyanage, D. Apul and M. J. Heben, *Energy Environ. Sci.*, 2017, **10**, 1297–1305.

47 J. Gong, S. B. Darling and F. You, *Energy Environ. Sci.*, 2015, **8**, 1953–1968.

48 G. Abbas, H. Assender, M. Ibrahim and D. Martin Taylor, *J. Vac. Sci. Technol. B Microelectron. Nanom. Struct.*, 2011, **29**, 052401.

49 M. Saliba, T. Matsui, J.-Y. Seo, K. Domanski, J.-P. Correa-Baena, N. Mohammad K., S. M. Zakeeruddin, W. Tress, A. Abate, A. Hagfeldt and M. Gratzel, *Energy Environ. Sci.*, 2016, **9**, 1989-1997.

50 N. K. Noel, S. N. Habisreutinger, B. Wenger, M. T. Klug, M. T. Hörantner, M. B. Johnston, R. J. Nicholas, D. T. Moore and H. J. Snaith, *Energy Environ. Sci.*, 2017, **10**, 145.

51 A. P. Grosvenor, M. C. Biesinger, R. S. C. Smart and N. S. McIntyre, *Surf. Sci.*, 2006, **600**, 1771–1779.

52 U. Diebold and T. E. Madey, *Surf. Sci. Spectra*, 1996, **4**, 227–231.

53 B. Erdem, R. A. Hunsicker, G. W. Simmons, E. D. Sudol, V. L. Dimonie and M. S. El-Aasser, *Langmuir*, 2001, **17**, 2664–2669.

54 R. Islam, G. Chen, P. Ramesh, J. Suh, N. Fuchigami, D. Lee, K. A. Littau, K. Weiner, R. T. Collins and K. C. Saraswat, *ACS Appl. Mater. Interfaces*, 2017, **9**, 17201–17207.

55 Z. Wang, J. Fang, Y. Mi, X. Zhu, H. Ren, X. Liu and Y. Yan, *Appl. Surf. Sci.*, 2018, **436**, 596–602.

56 B. Mustafa, J. Griffin, A. S. Alsulami, D. G. Lidzey and A. R. Buckley, *Appl. Phys. Lett.*,

2014, **104**, 4–9.

57 M. Wong-Stringer, O. S. Game, J. A. Smith, T. J. Routledge, B. A. Alqurashy, B. G. Freestone, A. J. Parnell, N. Vaenas, V. Kumar, M. O. A. Alawad, A. Iraqi, C. Rodenburg and D. G. Lidzey, *Adv. Energy Mater.,* 2018, **1801234**, 1–11.

58 Y. Bai, S. Xiao, C. Hu, T. Zhang, X. Meng, Q. Li, Y. Yang, K. S. Wong, H. Chen and S. Yang, *Nano Energy*, 2017, **34**, 58–68.

59 Y. Xie, K. Lu, J. Duan, Y. Jiang, L. Hu, T. Liu, Y. Zhou and B. Hu, *ACS Appl. Mater. Interfaces*, 2018, **10**, 14153–14159.

**Figures**

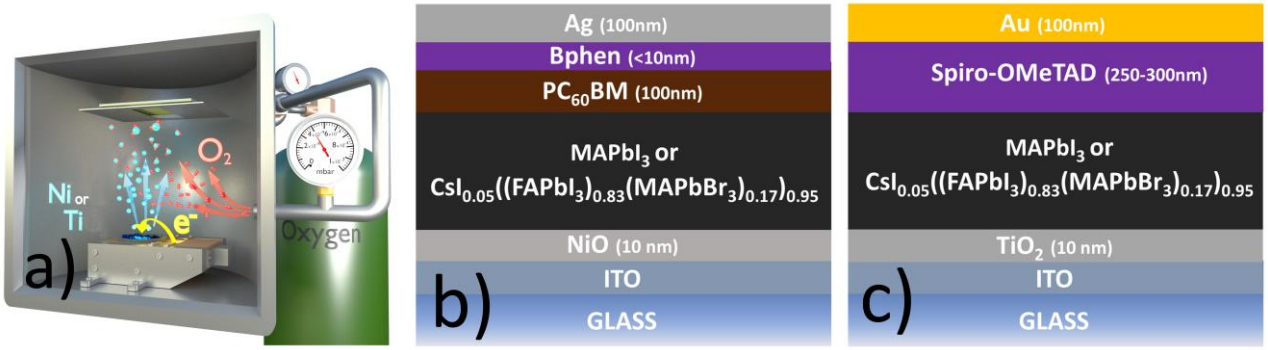


***Figure 1:*** *a) Reactive electron-beam deposition of metal oxides. The beam (yellow) heats the metal source material (blue) causing evaporation of the material (light blue), whilst oxygen (red) is fed into a vacuum system. The rate and oxygen partial pressure can be controlled. The substrate is rotated and covered with an evaporation mask. b) Inverted p-i-n perovskite solar cell used here, incorporating NiO deposited via reactive electron-beam deposition. c) Standard n-i-p perovskite solar cell used here, incorporating $TiO_2$ deposited via reactive electron-beam deposition.*

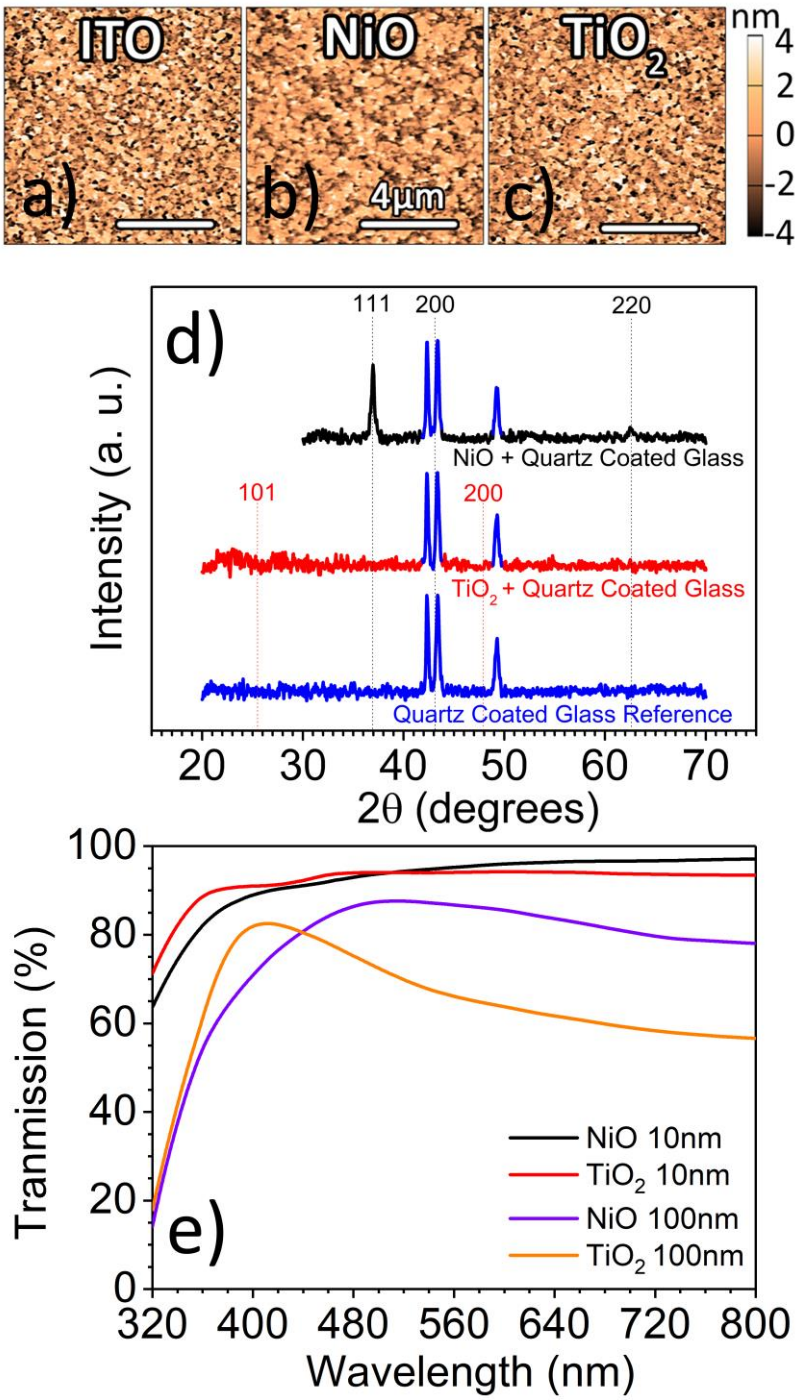


***Figure 2:*** *Characterisation of metal oxide films. Atomic force microscope topographs of a) ITO, b) ITO/NiO (10 nm) and c) ITO/$TiO_2$ (10 nm). d) X-ray diffraction patterns of our NiO and $TiO_2$ deposited onto quartz coated glass using the reactive e-beam process. Labelled dotted lines indicate known NiO and $TiO_2$ reflections with crystallographic planes labelled. e) Transmission UV-vis spectra of 10 nm and 100 nm NiO and $TiO_2$ films, deposited onto quartz coated glass using the reactive e-beam process.*

| p-i-n NiO AC | PCE [%] | $J_{SC}$ [mA/cm$^2$] | $V_{OC}$ [V] | FF [%] | $R_S$ [Ω] | $R_{SH}$ [Ω] |
|---|---|---|---|---|---|---|
| **10 nm NiO, 1 Å/s** | 11.5 ± 0.6 | 15.7 ± 0.8 | 1.05 ± 0.02 | 69.7 ± 3.0 | 6.05 ± 0.9 | 1540 ± 960 |
| **20 nm NiO, 1 Å/s** | 10.5 ± 1.1 | 16.5 ± 1.1 | 0.98 ± 0.02 | 64.1 ± 2.1 | 9.96 ± 1.7 | 1250 ± 630 |

***Table 1:*** *Performance metrics (average ± standard deviation) for p-i-n PSCs with a reactive e-beam deposited NiO HTM and AC perovskite active layer. PSCs are made with NiO thicknesses of 10 nm and 20 nm.*

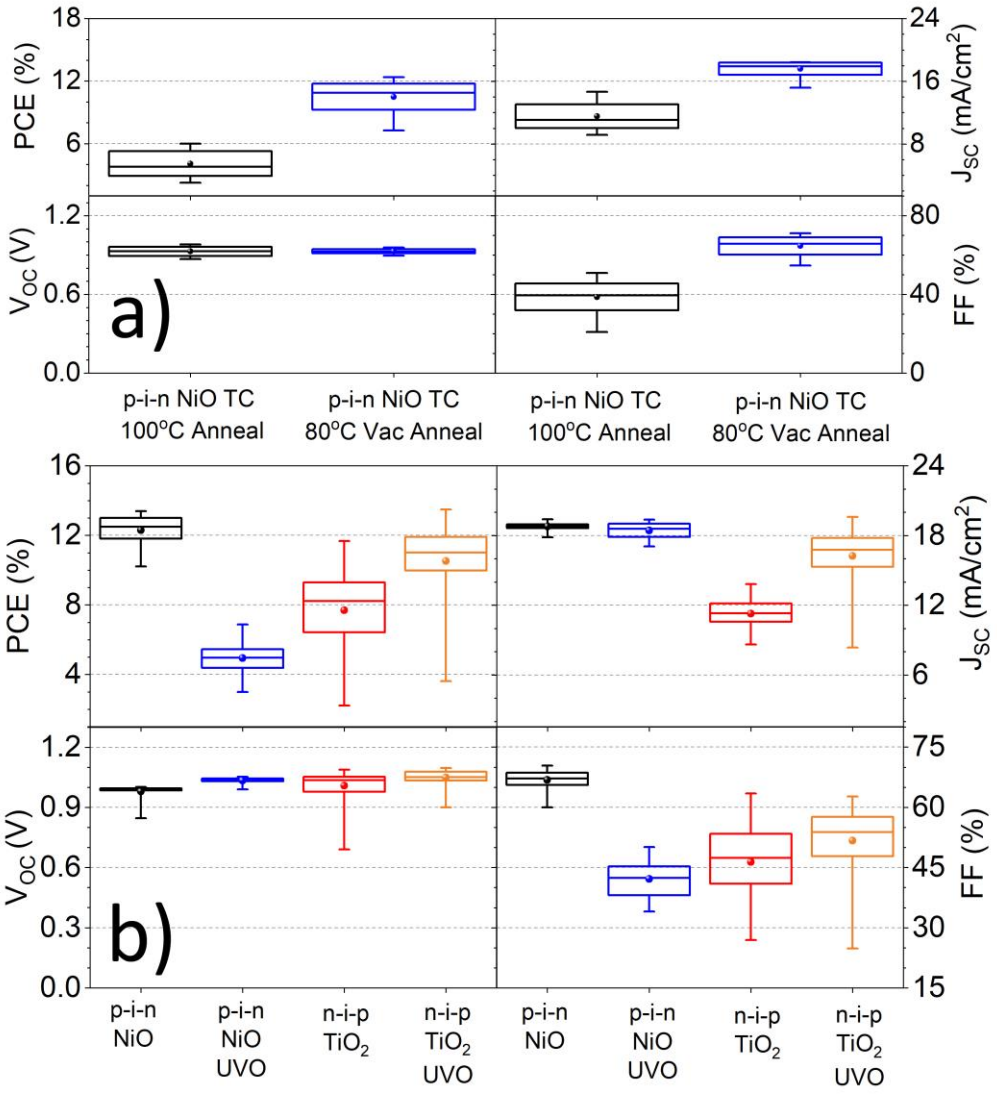


***Figure 3:*** *a) Box plot of performance metrics for p-i-n PSCs with a reactive e-beam deposited NiO HTM and TC active layer, PSCs are fabricated with a 100* °C *anneal (black) or an alternative 80* °C *vacuum anneal (blue) for conversion of the perovskite. b) Boxplots of performance metrics for p-i-n (black, blue) and n-i-p (red, orange) PSCs with reactive e-beam deposited NiO HTM and $TiO_2$ ETM respectively. The perovskite precursor is either deposited directly onto the metal oxides (black, red) or treated with UV-Ozone for 15 minutes (blue, orange) prior to deposition of the perovskite.*

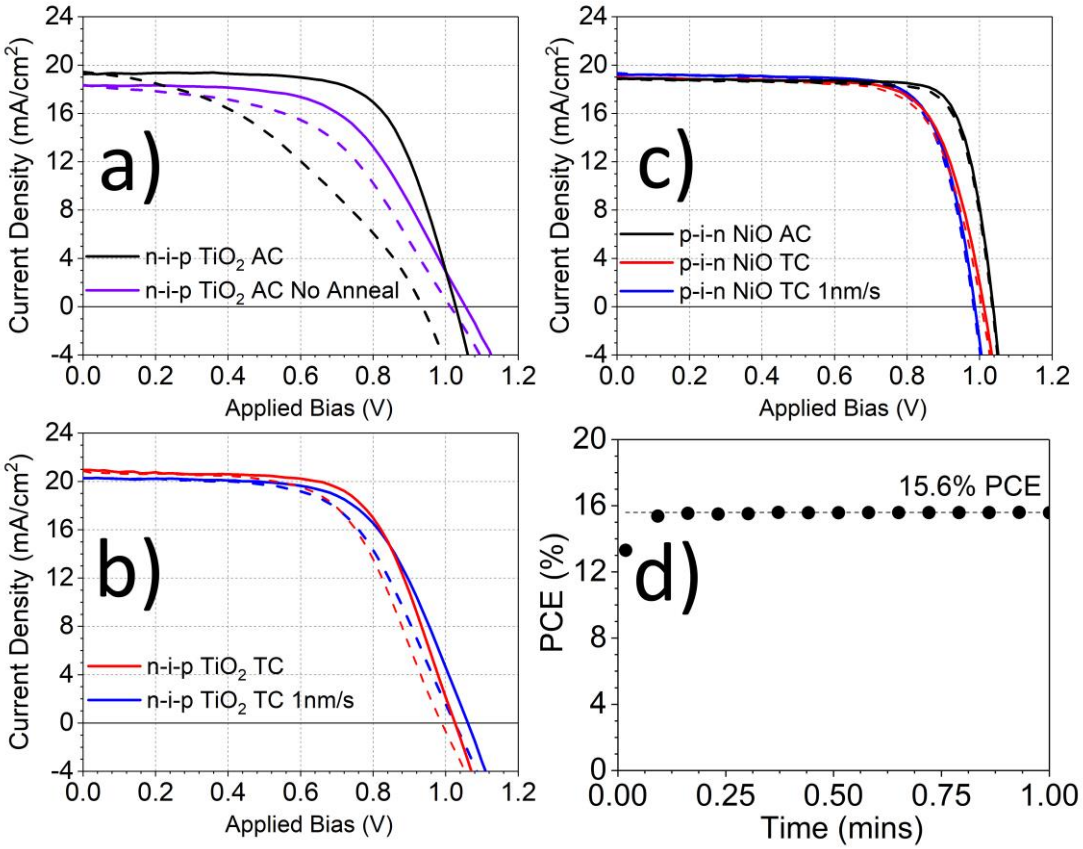


***Figure 4:*** *Current-Voltage sweeps for champion standard (n-i-p) and inverted (p-i-n) PSCs with AC and TC perovskite active layers. a) n-i-p with $TiO_2$ ETM and AC perovskite. b) n-i-p with $TiO_2$ ETM and TC perovskite. c) p-i-n with NiO HTM with AC and TC perovskite. Part a) also contains a champion n-i-p PSC without any anneal during fabrication (purple). For both architectures, PSCs with a TC perovskite and high rate of metal oxide evaporation (1 nm/s) are also included (blue). Dotted lines represent forward sweeps and solid lines represent reverse sweeps. d) A stabilised efficiency output for champion 15.8 % p-i-n with reactive e-beam deposited NiO and AC active layer.*

| | **p-i-n NiO AC** | **p-i-n NiO TC** | **p-i-n NiO 1 nm/s TC** | **n-i-p TiO2 AC** | **n-i-p TiO2 TC** | **n-i-p TiO2 1 nm/s TC** | **n-i-p TiO2 AC no Anneal** |
|---|---|---|---|---|---|---|---|
| PCE [%] | 15.8 | 14.0 | 14.2 | 13.6 | 13.9 | 13.5 | 11.3 |
| $J_{SC}$ [mA/cm$^2$] | 18.9 | 18.9 | 19.2 | 19.3 | 20.9 | 20.3 | 18.3 |
| $V_{OC}$ [V] | 1.04 | 1.01 | 0.99 | 1.03 | 1.03 | 1.06 | 1.05 |
| FF [%] | 80.5 | 73.0 | 74.8 | 68.6 | 64.8 | 62.5 | 58.4 |

***Table 2:*** *Performance metrics for champion p-i-n and n-i-p PSCs given in Figure 4.*